Wan *et al. Microstructures* 2023;3:2023014
DOI: 10.20517/microstructures.2022.36

Microstructures

Research Article

Open Access

The effect of chromium content on the corrosion behavior of ultrafine-grained $Cr_xMnFeCoNi$ high-entropy alloys in sulfuric acid solution

Tian Wan, Zhikun Huang, Zhuo Cheng, Mingyu Zhu, Weiwei Zhu, Zongyuan Li, Danni Fu, Fuzeng Ren

Department of Materials Science and Engineering, Southern University of Science and Technology, Shenzhen 518055, Guangdong, China.

Correspondence to: Prof. Fuzeng Ren, Department of Materials Science and Engineering, Southern University of Science and Technology, Shenzhen 518055, Guangdong, China. E-mail: renfz@sustech.edu.cn

How to cite this article: Wan T, Huang Z, Cheng Z, Zhu M, Zhu W, Li Z, Fu D, Ren F. The effect of chromium content on the corrosion behavior of ultrafine-grained $Cr_xMnFeCoNi$ high-entropy alloys in sulfuric acid solution. *Microstructures* 2023;3:2023014. https://dx.doi.org/10.20517/microstructures.2022.36

Received: 30 Oct 2022 **First Decision:** 1 Dec 2022 **Revised:** 6 Jan 2023 **Accepted:** 30 Jan 2023 **Published:** 22 Feb 2023

Academic Editors: Jun Chen, Shiqing Deng **Copy Editor:** Fangling Lan **Production Editor:** Fangling Lan

Abstract

Chromium (Cr) plays a critical role in the corrosion resistance of conventional alloys via the formation of a dense Cr oxide-based passive film. However, the exact role of Cr in the corrosion of high-entropy alloys (HEAs) remains unclear. The effect of Cr content on the corrosion behavior of the ultrafine-grained $Cr_xMnFeCoNi$ (x = 0, 0.6, 1, and 1.5) HEAs in the sulfuric acid solution (0.5 M H_2SO_4) was investigated. These HEAs were fabricated using a combination of mechanical alloying and spark plasma sintering. The electrochemical tests show that the passive film was more compact and thicker at higher Cr concentration, but the corrosion rate first increased and then decreased, due to the presence of the nanocrystalline-amorphous phase boundaries in the passive film. Long-time immersion tests show that the corrosion rate increased exponentially with the Cr content, due to the gradual accumulation of the galvanic corrosion.

Keywords: High-entropy alloy, polarization, galvanic corrosion, passive film

INTRODUCTION

High-entropy alloys (HEAs) have been reported with excellent mechanical properties at cryogenic temperatures[1-3] and high resistance to wear[4], irradiation[5] and corrosion[6,7], and are thus considered to be

© The Author(s) 2023. **Open Access** This article is licensed under a Creative Commons Attribution 4.0 International License (https://creativecommons.org/licenses/by/4.0/), which permits unrestricted use, sharing, adaptation, distribution and reproduction in any medium or format, for any purpose, even commercially, as long as you give appropriate credit to the original author(s) and the source, provide a link to the Creative Commons license, and indicate if changes were made.

promising candidates in extreme structural applications[8]. Among the HEAs, face-centered-cubic (fcc) CoCrFeMnNi HEA is of particular interest due to its excellent combination of high strength-ductility-toughness at cryogenic temperature[9-11]. For example, Gludovatz *et al.* reported that the CrMnFeCoNi HEA showed remarkable fracture toughness at cryogenic temperatures down to 77 K, comparable to the austenitic stainless steels and high Ni steels[10]. Such HEA and its sub-family generally have high Cr content, much above the required amount (12 at.%) to obtain "stainless" behavior on the surface for conventional corrosion-resistant alloys, such as stainless steel and nickel-based alloys[12], and thus, are expected to have superior corrosion resistance.

The mechanism of Cr to enhance the corrosion resistance of alloys is through the formation of a dense Cr oxide-based passive film[13,14], which serves as an effective barrier on an alloy across a wide range of pH[15]. There have been numerous reports on the corrosion behaviors of CoCrFeNi-based HEAs in recent few years[16-22]. Ye *et al.* found that the CrMnFeCoNi HEA coating showed nobler corrosion potential (E_{corr}) and lower corrosion current (I_{corr}) derived from the potentiodynamic polarization tests than 304 stainless steel (304SS) in a 0.5 M H_2SO_4 solution[21]. The AlCoCuFeNiCr HEA immersed in sulfuric acid solution showed better corrosion resistance than the Cr-free HEA, attributing to the formation of the compact Cr_2O_3 passive film on the surface[17]. However, the corrosion resistance of CrMnFeCoNi HEA was inferior when compared with 304 L stainless steel in a 0.1 M H_2SO_4 solution, because the passive film on the CrMnFeCoNi HEA was very unstable due to the low content of Cr and the extensive formation of metal hydroxide in the passive film[22]. Similar phenomena were also observed in several Cr-containing HEA systems, such as AlCoCrFeNi[18,19] and $FeCoNiCrCu_x$ HEAs[20]. For these HEAs, the distribution of Cr element in the matrix is relatively inhomogeneous and the Cr-depleted phase as anode would become a sensitive site to induce the formation of pitting. As a result, the general corrosion rate would be accelerated by the galvanic corrosion effect. Even with the same composition system of CoCrFeMnNi HEA, distinct corrosion behavior was observed[21-24]. Wang *et al.* found that the oxide film on HEA was duplex, comprising a Cr/Mn inner oxide layer and a Cr/Fe/Co outer oxide/hydroxide layer[25]. For now, the effect of Cr content on the corrosion mechanism in the HEAs has not been unraveled in detail. The matrix structure, composition, and the competing effect of the passive film and the pitting on the corrosion behavior can be revealed by exploring the Cr-containing HEAs with varying Cr concentrations.

In this work, the corrosion behavior of the $Cr_xMnFeCoNi$ (x = 0, 0.6, 1, and 1.5, respectively) HEAs with varying Cr concentrations in a 0.5 M H_2SO_4 solution was investigated. The matrix microstructure was characterized using X-ray diffraction (XRD), scanning electron microscopy (SEM) and transmission electron microscopy (TEM) in detail. Moreover, the corrosion behavior of the $Cr_xMnFeCoNi$ HEAs was examined using the potentiodynamic polarization tests and the electrochemical impendence spectroscope (EIS), along with the static immersion tests. Then, the corroded surface was analyzed using SEM, TEM, atomic force microscope (AFM) and X-ray photoelectron spectroscopy (XPS). Our main objective is to give an in-depth understanding of the effect of Cr on the corrosion behavior of the $Cr_xMnFeCoNi$ HEAs in sulfuric solution.

EXPERIMENTAL PROCEDURE

Alloy fabrication

The $Cr_xMnFeCoNi$ (x = 0, 0.6, 1, and 1.5) HEAs (hereafter denoted as Cr0, Cr0.6, Cr1, Cr1.5, respectively) were prepared using commercially pure (99.9 wt.%) elemental powder of Cr, Mn, Fe, Co and Ni as the starting material. The powder mixture was put into a stainless steel vial with a ball-to-powder mass ratio of 5:1 and subjected to high-energy ball milling for 9 h using a SPEX 8000D mill at ambient temperature in an argon glovebox. The ball-milled powders were consolidated by spark plasma sintering (SPS-211Lx,

Fujidempa Kogyo. Co., Ltd, Japan) at 950 °C for 5 min under a pressure of 45 MPa in vacuum condition (~ 6 Pa).

The sintered cylindrical HEAs were cut into discs using electrical discharge machining for subsequent characterization and tests. For electrochemical tests, the samples were cut into discs with a size of Φ = 10 mm × 3 mm, and sealed in epoxy with one surface exposed. The exposed surface was first mechanically ground using SiC paper down to 2400 grit, followed by vibratory polishing using a 0.06 μm alumina suspension. The polished samples were then cleaned with deionized water and alcohol and dried in air. For static immersion tests, both surfaces of the samples of the discs were ground and polished following the same procedure as those used for the electrochemical tests.

Microstructure characterization of the as-sintered HEAs

The phase of the as-sintered $Cr_xMnFeCoNi$ (x = 0, 0.6, 1, and 1.5) HEAs was identified using XRD patterns recorded on a Rigaku Smartlab-9KW diffractometer with Cu-Kα radiation (45 kV, 200 mA). The data were collected with 2θ in the range of 30° to 80° with a step size of 0.02° at a scanning speed of 10°/min. The surface morphology and composition were examined using SEM (TESCAN MIRA 3, Czech Republic) coupled with energy-dispersive X-ray spectroscopy (EDS). Electron backscatter diffraction (EBSD) was performed to characterize the grain structure of the HEAs. TEM (FEI Tecnai F30, USA) and high-angle annular dark-field scanning TEM (HAADF-STEM) were used to characterize the microstructure of the as-sintered HEAs. The TEM samples were prepared using site-specific focused ion beam (FIB; FEI Helios Nano Lab™ 600i) lift-out technique. Besides, platinum cap layers with a thickness of ~1 μm were deposited before milling the trench to protect the surface.

Electrochemical corrosion and immersion tests

Electrochemical measurements were performed in a 0.5 M H_2SO_4 solution at ambient temperature using a Princeton Applied Research Versa Studio (PARSTAT 4000A, Ametek Scientific Instruments, USA). A standard three-electrode cell system was performed during all the measurements using a platinum sheet as the counter electrode, a saturated calomel electron (SCE) as the reference electrode and the $Cr_xMnFeCoNi$ HEAs as the working electrode. Before EIS and potentiodynamic polarization tests, the specimens were subjected to the potentiostatic polarization at -0.6 V *vs.* SCE for 5 min to remove the surface oxidation, and then the open-circuit potential (OCP) was measured for 2 h in order to obtain a steady or quasi-steady potential value. EIS tests were performed at OCP with the sinusoidal potential amplitude of 10 mV in the frequency range from 100 kHz to 10 mHz. The data derived from EIS tests were fitted and analyzed using the Zsimpwin software. Then, the potentiodynamic polarization tests were conducted with the scanning range from -0.25 V *vs.* OCP to 1.3 V *vs.* SCE at a scan rate of 1 mV/s. Each electrochemical test was performed three times to confirm the reproducibility of the results.

The static immersion tests were performed in 0.5 M H_2SO_4 at ambient temperature for 15 days. Three parallel experiments were performed for each HEA. The average corrosion rate by mass loss C_w in mm/y was calculated using the following Eq. (1):

$$C_W = \frac{K\Delta W}{At\rho} \tag{1}$$

where k is the constant of 8.76×10^4, ΔW is the mass loss (g) after the immersion test, A is the surface area (cm^2), t is the immersion time (h), and ρ is the density (g/cm^3) of the sample, measured by Archimedes method.

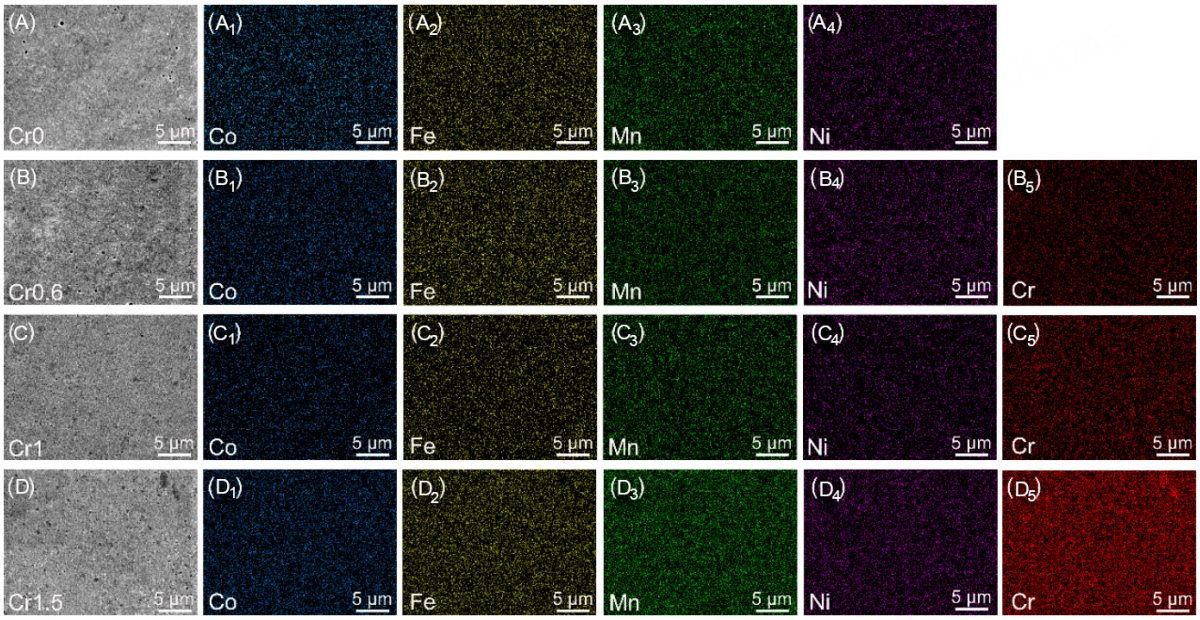

Figure 1. Surface morphology and EDS elemental maps of the as-sintered $Cr_xMnFeCoNi$ (x = 0, 0.6, 1, and 1.5) HEAs. (A-A_4) Cr0; (B-B_5) Cr0.6; (C-C_5) Cr1; and (D-D_5) Cr1.5. EDS: Energy-dispersive X-ray spectroscopy; HEAs: high-entropy alloys.

Corroded morphology and composition characterization

The corroded surface morphology was examined using SEM and AFM (Dimension edge, Bruker Corporation, Germany). The surface composition was analyzed using EDS and XPS (Thermo Scientific K-Alpha$^+$). The standard C 1s spectrum at a binding energy of 284.8 eV was employed to calibrate the original peaks, and the calibrated XPS data were analyzed and fitted by the software Avantage 5.9. TEM and HAADF-STEM coupled with EDS were used to analyze the typical corrosion micropores at the surface.

RESULTS

Phase, composition and microstructure of the as-sintered HEAs

The measured density of all the sintered $Cr_xMnFeCoNi$ HEAs exceeds ~ 98%. Very few pores were located on the surface [Figure 1A-D], confirming the high density of the HEAs. Some randomly distributed tiny dark spots were found on the surface. EDS line scanning profiles [Supplementary Figure 1] show that such dark spots are rich in Cr, Mn and O. EDS elemental maps [Figure 1] show the uniform distribution of Co, Fe, Mn and Ni, while Cr shows segregation and inhomogeneity. With a higher concentration of Cr, the Cr-rich region in the HEA is more obvious. Quantitative EDS analysis [Table 1] shows that the sintered HEAs have very close compositions to the nominal input ones.

XRD patterns of the $Cr_xMnFeCoNi$ HEAs [Figure 2] show that the spark-plasma-sintered HEAs have a dominant fcc matrix phase with a trace amount of (Cr, Mn)O_x oxides owing to the relatively low vacuum during the sintering process and the high chemical activity of Cr and Mn. The oxide phase content increases with the Cr concentration. The XRD patterns confirmed that the tiny dark particles found on the surface were oxides. EBSD inverse pole figure (IPF) maps [Figure 3] show that the $Cr_xMnFeCoNi$ HEAs have equi-axed grain structure and very similar average grain size, in the range of 312 to 360 nm. Furthermore, TEM-based techniques were used to characterize the microstructure in more detail. The HAADF-STEM image [Figure 4A] shows three contrasts. A considerable number of nano-sized precipitates in grey contrast are distributed at the grain boundaries and inside the grains of the matrix, where a few black precipitates are

Table 1. Quantitative EDS analysis (in atomic percentage) for the as-sintered $Cr_xMnFeCoNi$ (x = 0, 0.6, 1, and 1.5) HEAs

Sample	Co	Fe	Mn	Ni	Cr
Cr0	25.0	25.4	25.0	24.6	-
Cr0.6	21.7	21.7	22.3	21.1	13.2
Cr1	19.4	20.3	20.2	19.7	20.4
Cr1.5	18.1	18.2	18.4	18.1	27.2

EDS: Energy-dispersive X-ray spectroscopy; HEAs: high-entropy alloys.

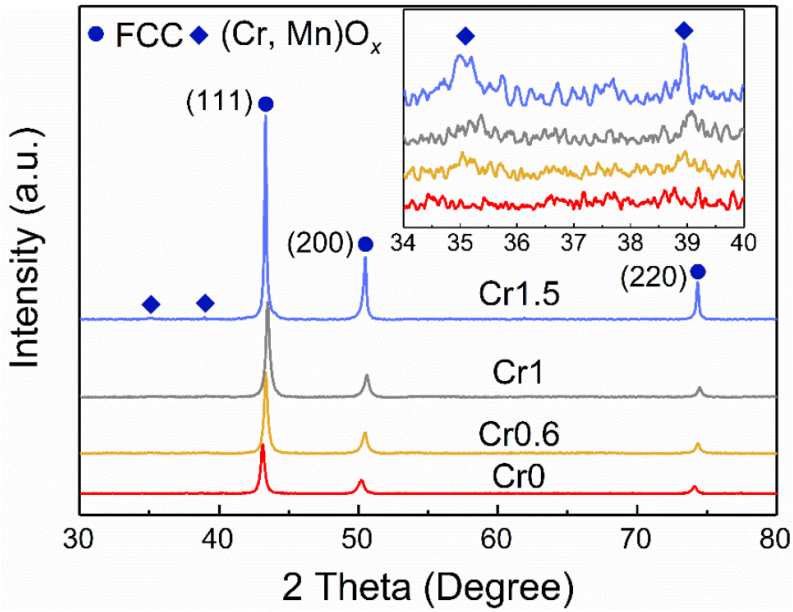

Figure 2. XRD patterns of the $Cr_xMnFeCoNi$ (x = 0, 0.6, 1, and 1.5) HEAs. XRD: X-ray diffraction; HEAs: high-entropy alloys.

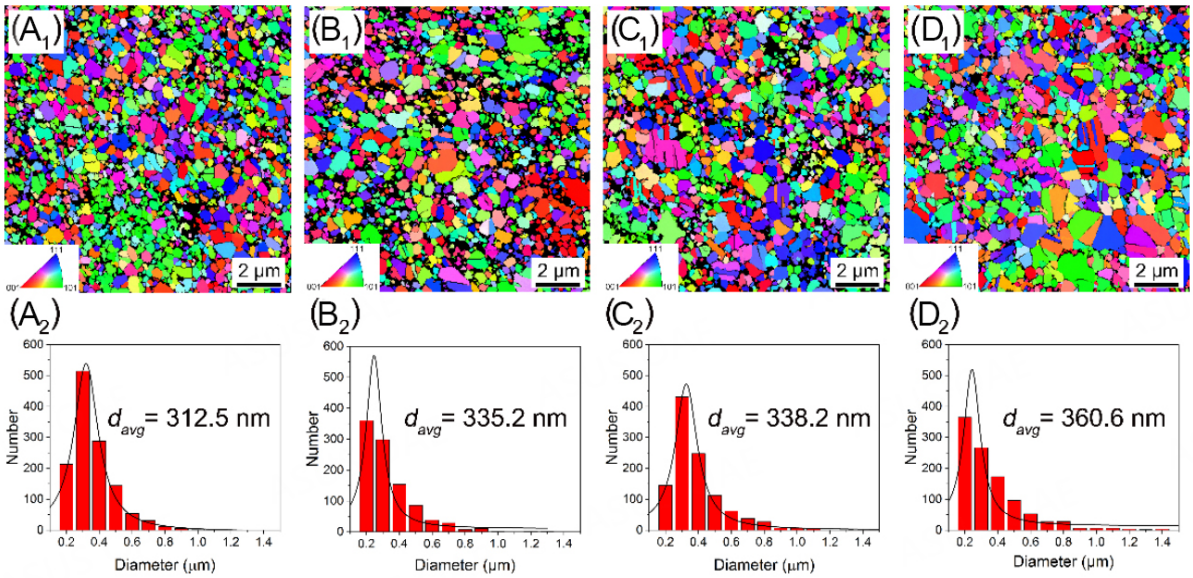

Figure 3. EBSD IPF maps and the average grain size distribution of the as-sintered $Cr_xMnFeCoNi$ (x = 0, 0.6, 1, and 1.5) HEAs. (A) Cr0, (B) Cr0.6, (C) Cr1 and (D) Cr1.5. EBSD: Electron backscatter diffraction; IPF: inverse pole figure; HEAs: high-entropy alloys.

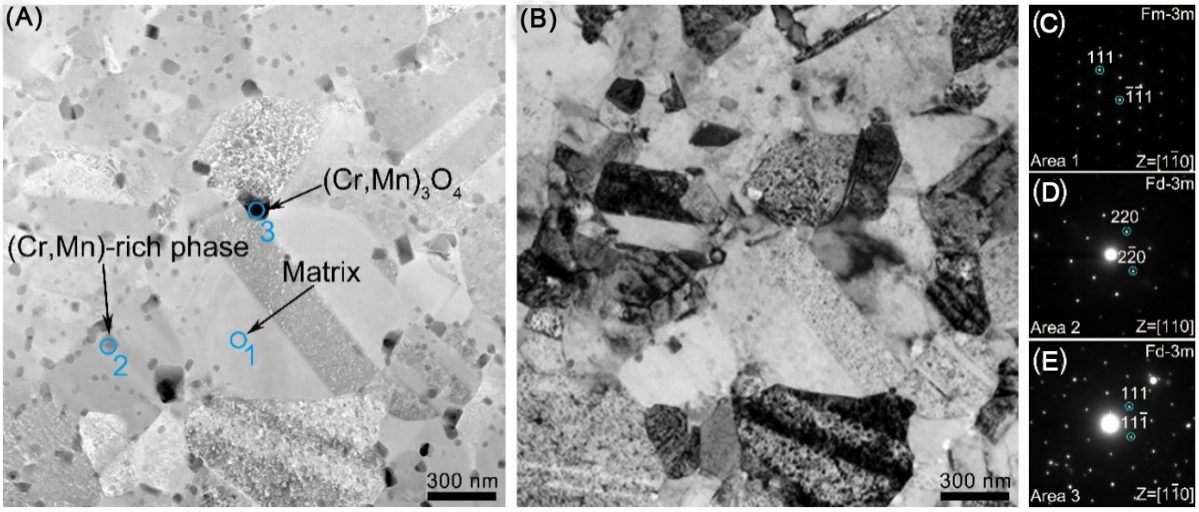

Figure 4. TEM characterization of the as-sintered CrMnFeCoNi (Cr1, *x* = 1) HEA. (A and B) are HAADF-STEM and corresponding bright-field TEM images; (C-E) are SAED patterns of the matrix, the grey precipitate and the black precipitate in (A), respectively. TEM: Transmission electron microscopy; HEA: high-entropy alloy; HAADF-STEM: high-angle annular dark-field scanning TEM; SAED: selected area electron diffraction.

located only at the grain boundaries. EDS quantitative analysis [Table 2] reveals that the matrix is depleted in Cr, while the grey precipitates are rich in Cr and Mn, and the black precipitates were identified to be (Cr, Mn)O_x, as detected in the XRD pattern in Figure 2. Bright-field TEM image [Figure 4B] clearly shows the microstructure of the Cr1 HEA. Selected area electron diffraction (SAED) patterns [Figure 4C-E] show that the matrix belongs to the Fm-3m space group, while both precipitates are in Fd-3m space group, consistent with the recent study[26] that also reported that the (Cr, Mn)O_x phase belonged to the Fd-3m space group in the Cr1 HEA fabricated using medium frequency induction melting. Combined with the EDS quantitative analysis, the black precipitates were identified to be (Cr, Mn)$_3O_4$.

Potentiodynamic polarization

Figure 5 shows the potentiodynamic polarization curves of Cr_xMnFeCoNi HEAs in a 0.5 M H_2SO_4 at room temperature. The values of E_{corr} and I_{corr} derived from the polarization curves were included in Table 3. With the increase of the Cr concentration, the E_{corr} shows more negative value from -0.40 V to -0.45 V, which suggests a more severe corrosion tendency, but not the actual corrosion rate at the moment in terms of kinetics[27,28]. The increment in the corrosion sensitivity may be due to the presence of more Cr-rich phases and the oxides precipitated in the matrix. In comparison with the CoFeMnNi HEA (Cr0) in the absence of the Cr, the I_{corr} of Cr0.6 HEA first increases and then gradually decreases with the increasing Cr concentration. The Cr0.6 HEA shows the highest I_{corr} of 5.36 μA/cm^2 and the Cr1.5 HEA shows the lowest I_{corr} of 2.75 μA/cm^2. Since the corrosion rate is positively correlated to I_{corr}, Cr0.6 has the lowest corrosion resistance, which may be attributed to the galvanic corrosion between the Cr-rich phase and the matrix as well as the lack of protection from the passive film. On the contrary, the Cr1.5 HEA has the highest corrosion resistance. However, when the applied potential reaches ~ 0.8 V, the current density of Cr1.5 increases faster than Cr0, suggesting that the Cr1.5 HEA has inferior pitting resistance.

Surface morphology and composition after polarization tests

After potentiodynamic polarization tests in the 0.5 M H_2SO_4 solution at room temperature, the Cr_xMnFeCoNi HEAs surfaces were covered with uniformly distributed micro-and nano-pores [Figure 6]. The average size of the pores increased, but the number reduced on the corroded surfaces of the HEAs with

Table 2. Quantitative EDS analysis (in atomic percentage) of Cr1 HEA in Figure 4A

Point	O	Cr	Mn	Fe	Co	Ni
1	-	16.3	21.3	21.6	19.8	21.0
2	10.4	26.4	22.1	13.4	13.3	14.4
3	47.3	31.1	21.6	-	-	-

EDS: Energy-dispersive X-ray spectroscopy; HEA: high-entropy alloy.

Table 3. Polarization parameters and equivalent circuit parameters for EIS of $Cr_xMnFeCoNi$ (x = 0, 0.6, 1 and 1.5) HEAs in a 0.5 M H_2SO_4 solution

Sample	E_{corr}/V	I_{corr}/μA/cm^2	Y_p/S·cm^{-2}·s^n	n_p	R_p/Ω·cm^2	*chsq*
Cr0	-0.40 ± 0.01	4.20 ± 0.08	2.60E-08	0.74	6113	2.28E-04
Cr0.6	-0.41 ± 0.03	5.36 ± 1.05	1.25E-08	0.79	3510	1.47E-04
Cr1	-0.44 ± 0.01	3.33 ± 1.61	9.35E-09	0.84	5506	1.85E-04
Cr1.5	-0.45 ± 0.01	2.75 ± 1.41	1.11E-08	0.82	7715	5.73E-04

EIS: Electrochemical impendence spectroscope; HEAs: high-entropy alloys.

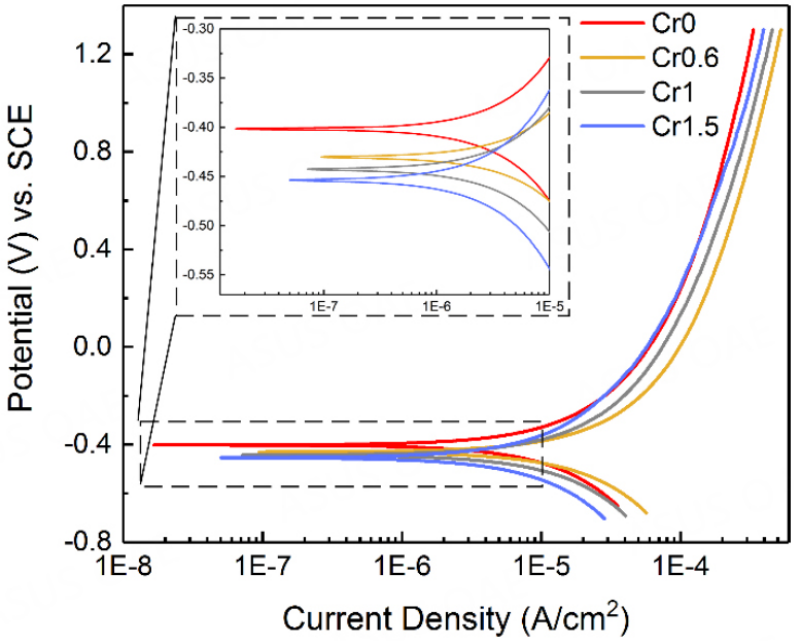

Figure 5. Potentiodynamic polarization curves of the as-sintered $Cr_xMnFeCoNi$ (x = 0, 0.6, 1, and 1.5) HEAs in a 0.5 M H_2SO_4 solution at room temperature.

a higher concentration of Cr, suggesting stronger tendency towards localized corrosion. AFM height images [Figure 6A3-D3] show that the depth of pores is in the range of 170 - 360 nm for Cr0, Cr0.6, and Cr1 HEAs. The Cr1 HEA shows the smallest depth of pores of ~ 180 nm, which might be attributed to the enhanced protective effect of the passive film to inhibit further corrosion from the etching solution. However, the surface micropores of the Cr1.5 HEA show much larger depth and reach ~1 μm, which could be liable to cause galvanic corrosion in the deep regions.

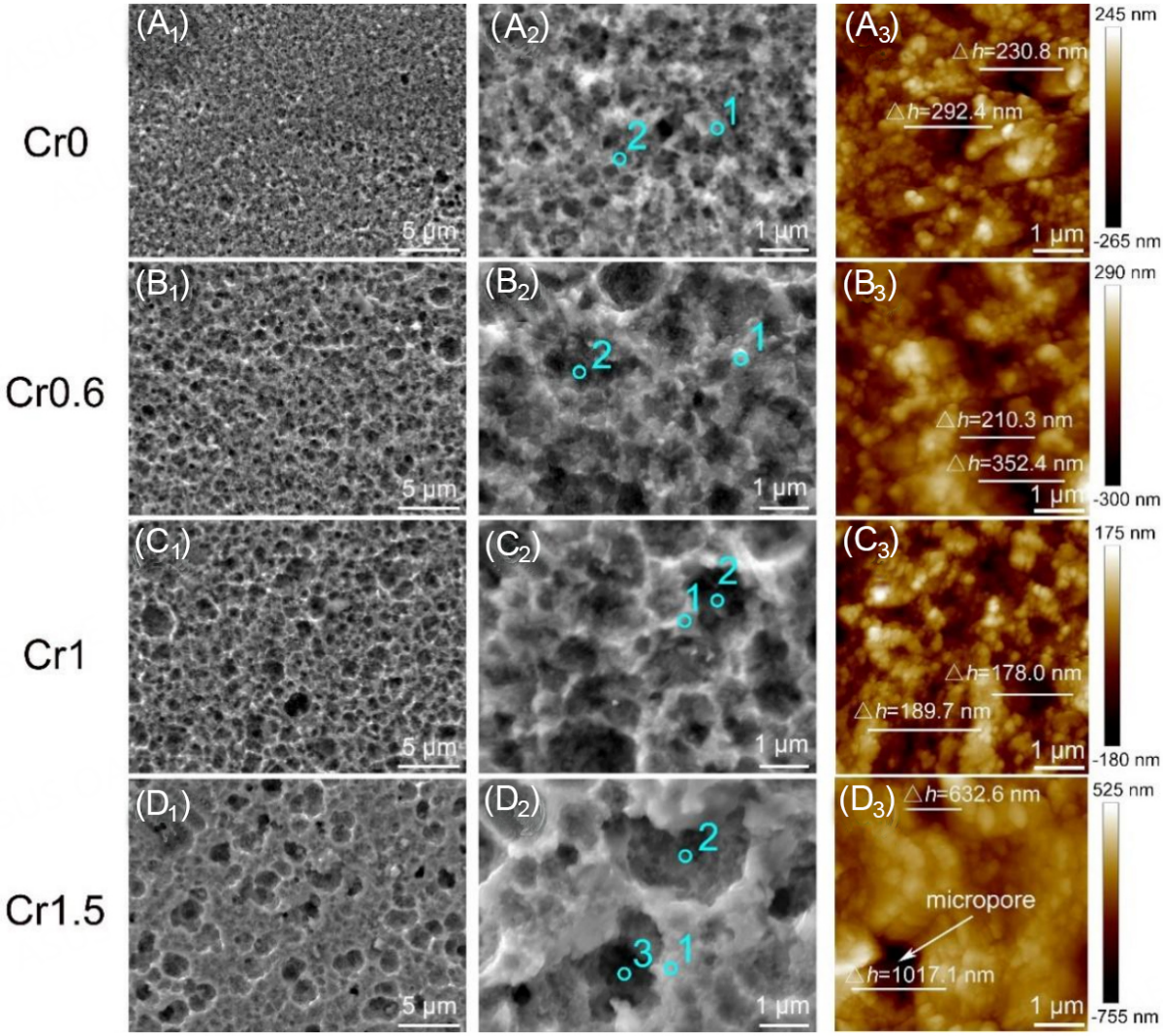

Figure 6. Surface morphology (A_1-D_1, A_2-D_2) and AFM height images (A_3-D_3) of the $Cr_xMnFeCoNi$ (x = 0, 0.6, 1, and 1.5) HEAs after polarization tests in a 0.5 M H_2SO_4 solution at room temperature.

Quantitative EDS analysis on the honeycomb-like surface of $Cr_xMnFeCoNi$ HEAs [Figure 6A2-D2] is included in Table 4. Inside the pores, all the four groups of HEAs have reduced content of Fe, Co and Ni but increased O, suggesting the selective dissolution of the elements Fe, Co and Ni and the formation of oxide films occurred simultaneously during the corrosion process. It is noted that the peak positions (point 1, Figure 6D2) of the Cr1.5 HEA surface contain a much higher content of O, indicating a better passivation effect on the region outside the micropores. However, the content of O in the deep valley of the pores (point 3, Figure 6D2) is lower than the shallow ones (point 2, Figure 6D2), and much lower than the peak positions (point 1, Figure 6D2), suggesting that the formation of oxide films was inhibited in the deep micropores. Hence, the region inside the deep micropores (point 3, Figure 6D2) of the Cr1.5 HEA would have the worst pitting corrosion resistance, as also confirmed by the content of selective dissolution elements. Furthermore, the corrosion behavior would be deteriorated due to the weak sites in sufficiently deep micropores during further corrosion and could cause pitting-like corrosion[29,30].

Table 4. Quantitative EDS analysis (in atomic percentage) on the corroded surface of $Cr_xMnFeCoNi$ (x = 0, 0.6, 1, and 1.5) HEAs in Figure 6

Sample	Point	O	Cr	Mn	Fe	Co	Ni
Cr0	(a_2)-1	-	-	24.8	25.0	25.6	24.6
	(a_2)-2	8.3	-	24.0	23.4	23.3	21.0
Cr0.6	(b_2)-1	5.9	12.5	20.3	20.6	20.2	20.5
	(b_2)-2	14.2	14.9	20.0	17.3	16.5	17.1
Cr1	(c_2)-1	-	20.3	19.9	20.3	20.1	19.4
	(c_2)-2	13.5	18.0	17.7	17.2	17.0	16.6
Cr1.5	(d_2)-1	16.0	24.6	16.8	14.5	13.6	14.5
	(d_2)-2	7.1	27.6	18.0	16.0	15.6	15.7
	(d_2)-3	2.4	34.0	23.8	14.7	12.8	12.3

EDS: Energy-dispersive X-ray spectroscopy; HEAs: high-entropy alloys.

XPS was performed to identify the chemical state of the corrosion products on the corroded surface of $Cr_xMnFeCoNi$ HEAs after polarization tests. The high-resolution XPS spectra and the quantitative analysis results were presented in Figure 7 and Table 5, respectively. For all the four groups of HEAs, the Co $2p_{3/2}$ spectrum is split into four constituent peaks, including Co (778.3 eV), CoO (780.2 eV), Co_2O_3 (781.3 eV), and $Co(OH)_2$ (782.1 eV). In addition, a Fe LM2 peak at 783.7 eV was also detected. The Fe $2p_{3/2}$ spectrum can be divided into four peaks as Fe at 707 eV, FeO at 709.3 eV, Fe_2O_3 at 710.8 eV, $Fe(OH)_3$ at 711.3 eV along with the Co LM2 at 712.7 eV, but the Fe in Cr0 HEA shows much lower intensity [Figure 7A2] compared with the Cr-containing HEAs. The Mn $2p_{3/2}$ spectrum is separated into four peaks as Mn at 638.8 eV, MnO at 640.5 eV, Mn_2O_3 at 641.5 eV, and MnO_2 at 642.6 eV along with Ni LM2 at 640.7 eV. The relative content of Mn oxides is larger than that of Co, Fe and Ni, especially for Cr0 and Cr1.5 HEAs. The Ni $2p_{3/2}$ spectrum is separated into four peaks with Ni at 853 eV, NiO at 854.2 eV, $Ni(OH)_2$ at 855.5 eV and Ni_{sat} at 859.4 eV. Based on the relative intensity of each element, it is concluded that the corroded surfaces are mainly composed of the metallic Ni and Co and small amounts of oxides/hydroxides. The Cr0 and Cr1.5 HEAs contain more Fe oxides/hydroxides. Moreover, the Cr $2p_{3/2}$ spectrum for Cr-containing HEAs is separated into three peaks as Cr at 574.2 eV, Cr_2O_3 at 576.1 eV and $Cr(OH)_3$ at 577.1 eV. The relative contents of Cr oxide and hydroxide are obviously higher compared to those of Co, Fe and Ni for Cr1.5 HEA.

Compared with Cr0 HEA in the absence of Cr, the Cr0.6 HEA shows significantly reduced content of Fe and Mn oxides/hydroxides in the oxide film, which thus shows weaker corrosion resistance. Likewise, as the Cr concentration increases from Cr 0.6 to Cr1.5, the increased amount of oxide/hydroxide of Cr, Mn and Fe provides denser and more protective oxide film for Cr1.5 HEA than Cr0.6 and Cr1 HEAs. However, the enrichment of Mn in the oxide film could degrade the stability of the passive film[31], which could lead to the breakdown of the oxide film in the local region of the Cr1.5 HEA during severe corrosion. On the whole, the quantitative analysis results suggest that Co and Ni are preferentially dissolved, which are in agreement with the results of the EDS point analysis in Table 4. The content of Fe does not reduce obviously for Cr0, Cr0.6 and Cr1, except for Cr1.5, showing that the selective dissolution of Fe is more difficult than Co and Ni. It also demonstrates that Cr oxide (Cr_2O_3) and hydroxide ($Cr(OH)_3$) are indeed generated on the surfaces of Cr-containing HEAs in the nominal Cr concentration of ~13.0 at.% at least, which is close to the threshold in conventional stainless steels[12].

In order to clarify the honeycomb-like structure of the surface, the cross-sectional microstructure of a typical corrosion micropore located on the surface of Cr1 was characterized by TEM in detail, as shown in

Table 5. The quantitative analysis (in atomic percentage) of the XPS spectra of the corroded surface on Cr0, Cr0.6, Cr1 and Cr1.5 in Figure 7

Spectrum	Substance	Cr0	Cr0.6	Cr1	Cr1.5
Co $2p_{3/2}$	Co	13.4	17.6	15.6	9.0
	CoO	2.8	0.2	0.9	0.9
	Co_2O_3	2.1	0.2	1.1	0.2
	$Co(OH)_2$	3.7	1.9	3.0	1.1
Fe $2p_{3/2}$	Fe	10.1	19.3	16.2	10.2
	FeO	11.0	0.3	1.6	1.1
	Fe_2O_3	3.6	0.7	2.0	3.8
	$Fe(OH)_3$	2.3	1.3	1.2	-
Mn $2p_{3/2}$	Mn	3.8	11.0	12.4	3.6
	MnO	3.4	2.1	2.1	4.2
	Mn_2O_3	10.1	6.8	4.2	10.0
	MnO_2	8.7	1.9	2.4	2.9
Ni $2p_{3/2}$	Ni	15.1	13.4	12.7	8.4
	NiO	4.6	1.8	2.2	1.8
	$Ni(OH)_2$	5.3	3.2	2.7	4.3
Cr $2p_{3/2}$	Cr	-	12.1	15.7	13.7
	Cr_2O_3	-	1.8	2.6	18.4
	$Cr(OH)_3$	-	4.4	1.4	6.4

Figure 8. The depth of the micropore is ~200 nm, in line with the result of the AFM height image in Figure 6. Furthermore, the selected cross-section can clearly be divided into two regions. The top region above the interface (the dotted line in Figure 8A) is referred to as the oxide film inside the micropore, while the region below the interface is the un-corroded matrix. High-resolution TEM image [Figure 8A] along with fast Fourier transform (FFT) patterns [Figure 8B and C] reveals that the oxide film consists of both amorphous and nanocrystalline (Cr, Mn)O_x. The boundaries between the nanocrystalline and the amorphous phases are considered to provide tunnels for species diffusion and transport, where the corrosive ions permeate preferentially, similar to the mechanism that the Cl^- ion attacks on the oxide film of the metals[32]. It might be induced by the detrimental effect of Mn, which could be concentrated in the oxide film to greatly affect the occurrence of the nanocrystalline phase. The EDS elemental maps [Figure 8E] indicate that the oxide film is rich in Mn, Cr and O, but deficient in Fe, Co and Ni.

EIS

To understand the corrosion mechanism of Cr_xMnFeCoNi HEAs in the 0.5 M H_2SO_4 solution, the EIS measurements under OCP conditions were conducted and analyzed in Figure 9. In terms of the Nyquist plots [Figure 9A], all HEAs have similar features where a depressed capacitive semicircle covers high frequency region and some scattered points are distributed randomly near the real axis in the low frequency region. The diameter of the capacitive semicircle first decreases from Cr0 to Cr0.6 and then increases to Cr1.5, indicating the same trend for the corrosion resistance[22,33]. It is found that only one time constant is presented in the high frequency of each Bode plot [Figure 9B], indicating the corrosion behavior of the passive film. With the decrease of the frequency, the phase angle reduces. The capacitance for the passive film increases and the corrosion resistance decreases, suggesting that the etching solution gradually sinks into the passive film. Moreover, in the wide range of the low frequency region, the phase angles are all approximately 0° and the values of $|Z|$ are constant, which are characteristic of the pure resistance, indicating that the passive films on the HEAs are not very compact. Likewise, the value of $|Z|$ at a fixed frequency of 0.1 Hz is usually equal to the polarization resistance related to the corrosion resistance[34].

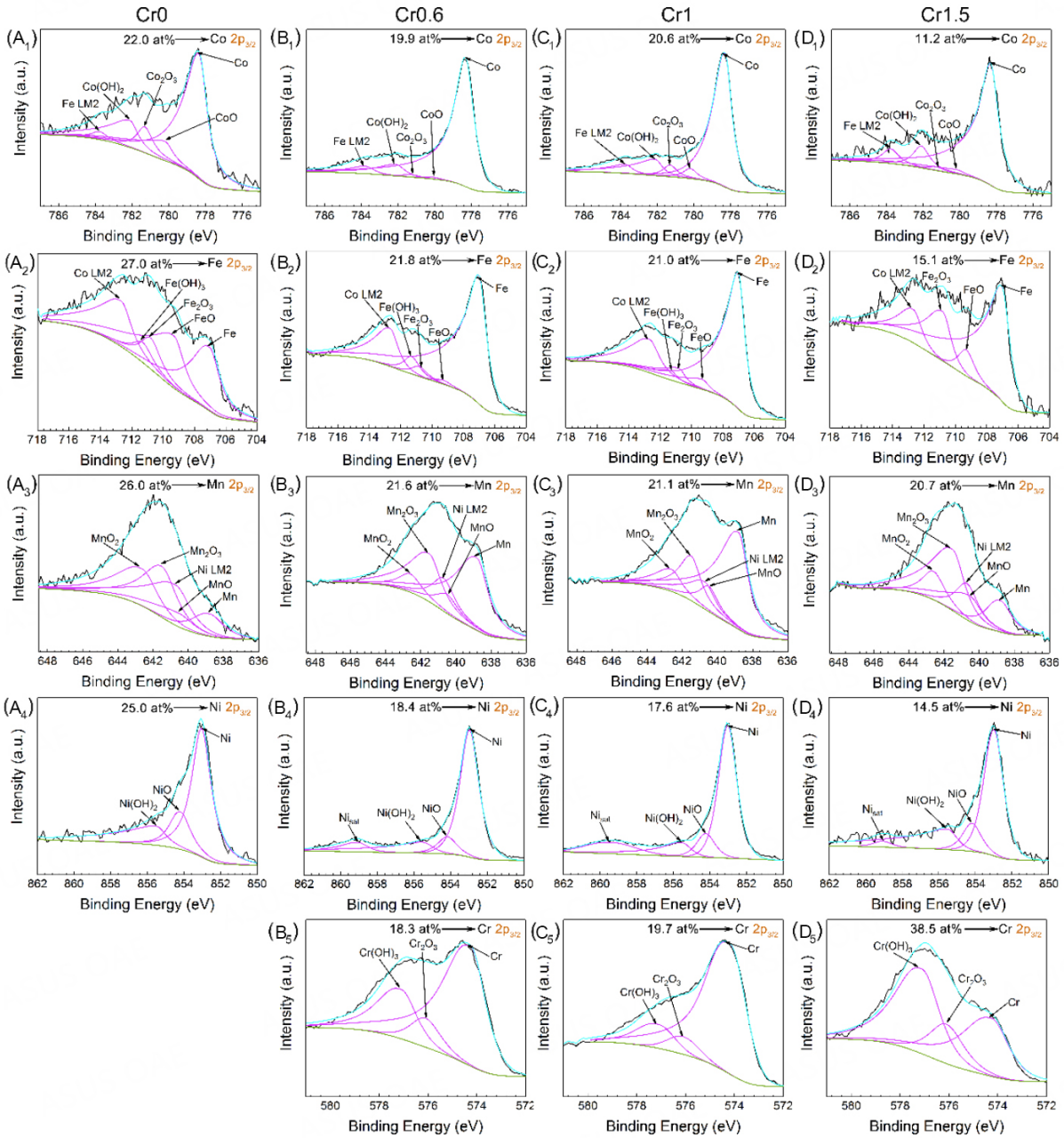

Figure 7. High-resolution XPS spectra of the corroded surface on Cr0 (A_1-A_4), Cr0.6 (B_1-B_5), Cr1 (C_1-C_5), and Cr1.5 (D_1-D_5) HEAs after polarization in a 0.5 M H_2SO_4 solution at room temperature. (A_1-D_1) Co $2p_{3/2}$; (A_2-D_2) Fe $2p_{3/2}$; (A_3-D_3) Mn $2p_{3/2}$; (A_4-D_4) Ni $2p_{3/2}$; and (B_5-D_5) Cr $2p_{3/2}$. XPS: X-ray photoelectron spectroscopy.

Therefore, the corrosion resistance follows the order of Cr1.5 > Cr0 > Cr1 > Cr0.6. On the other hand, there is no straight line representing the diffusion process or another capacitive semicircle corresponding pitting behavior present in the Nyquist plot, which is due to the simultaneous formation of the passive film at the corroded region when the etching solution reaches the matrix [Figure 6].

In order to fit the results of the EIS under the OCP condition, an electrical equivalent circuit (EEC) model (inset in Figure 9A) was used. In the EEC model, a parallel combination of a constant phase element Q_p and

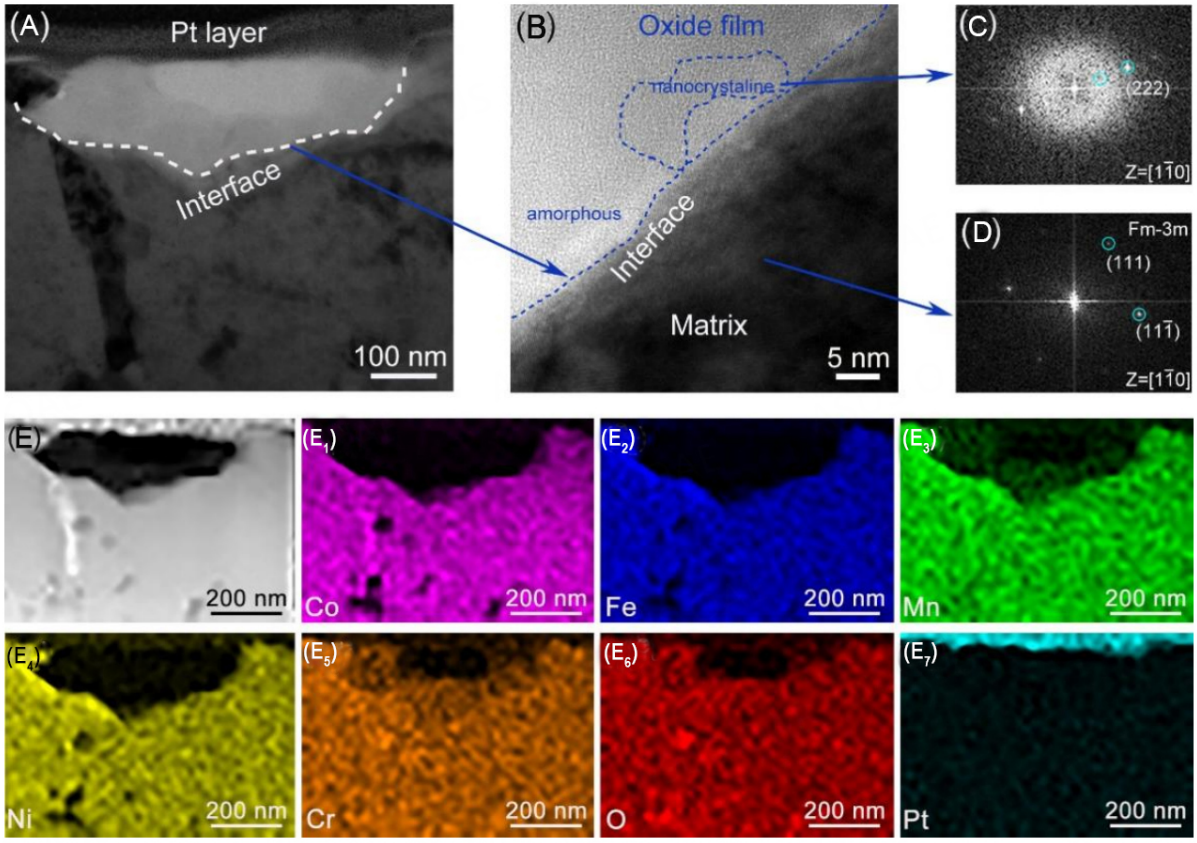

Figure 8. TEM characterization of a typical corrosion micropore on the surface of Cr1 HEA. (A) Bright-field TEM image; (B-D) are the high-resolution TEM image obtained from the interface region and the corresponding FFT patterns, respectively; and (E-E$_7$) HAADF-STEM image with the corresponding EDS elemental maps. TEM: Transmission electron microscopy; HEA: high-entropy alloy; FFT: fast fourier transform; HAADF-STEM: high-angle annular dark-field scanning TEM; EDS: energy-dispersive X-ray spectroscopy.

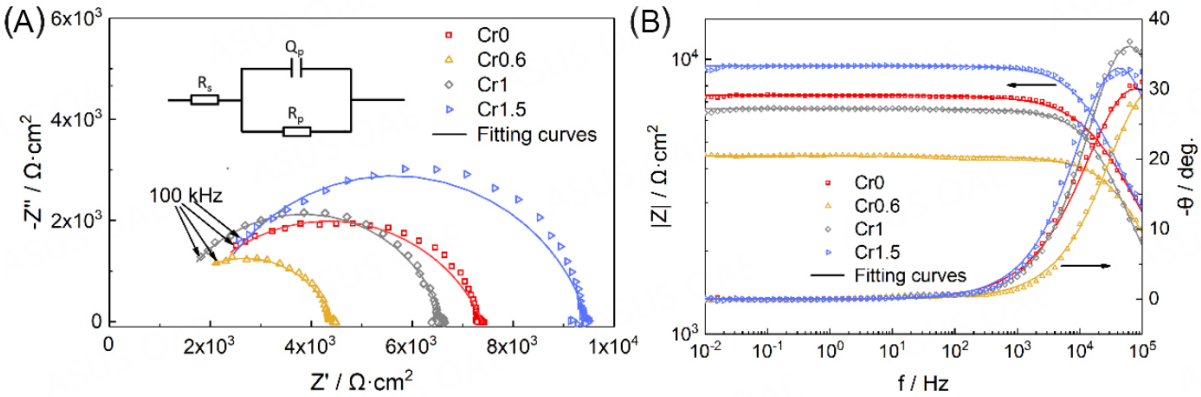

Figure 9. Nyquist (A) and Bode plots (B) of the Cr$_x$MnFeCoNi (x = 0, 0.6, 1, and 1.5) HEAs in a 0.5 M H_2SO_4 solution under open circuit potential condition. The inset in (A) is the electrical equivalent circuit (EEC) for fitting the EIS results. HEAs: High-entropy alloys; EIS: electrochemical impendence spectroscope.

a passivation layer resistance R_p corresponding to one time constant is in series with a solution resistance R_s, which has good fitting reliability as the small chi-square values in the order of magnitudes of 10^{-4} listed in Table 3. Herein, the ideal capacitance C_p is replaced by the constant phase element Q_p to compensate for the

non-homogeneity and the capacity dispersion in the system[35], such as an uneven corroded surface. The Q_p impendence Z_Q is given as follows,

$$Z_Q = Y_p^{-1}(j\omega)^{n_p} \tag{2}$$

Where Y_p is the proportionality factor, j is the imaginary unit, ω is the phase frequency, and n is the phase shift, reflecting the degree of the dispersion for an ideal capacitance. For n_p = 1, Z_Q represents a pure capacitance with $C_p = Y_p$; for n_p = 0.5, it presents a Warburg resistance; and for n_p = 0, it presents a pure resistance with $R_p = Y_p^{-1}$. As a result, n_p increases from Cr0 to Cr1, implying that the passive film becomes more compact on the surface. While from Cr1 to Cr1.5, n_p decreases slightly, which is ascribed to the discontinuous passive film containing the weak site in the deep micropore, as shown in Figure 6. Moreover, as the value of n_p is in the range of 0.74-0.84, which is close to 1, the value of Y_p can be approximately regarded as capacitance C_p of the passive film. Considering the Helmholtz model[21,36], the value of Y_p is determined by the equation as follows,

$$Y_p \approx C_p = \frac{\varepsilon\varepsilon_0}{d}S \tag{3}$$

where d is the thickness of the passive film, S is the exposed surface area, ε_o is the permittivity of the vacuum, and ε is the dielectric constant of the surface which is mainly determined by the composition of the passive film. Therefore, the decrease of the value of Y_p from Cr0 to Cr1 and then the increase from Cr 1 to Cr1.5 can be affected by two factors for all samples: the change of the composition and the thickness of the passive film. Meanwhile, as Cr0.6 and Cr1 have a similar surface composition as analyzed by XPS [Figure 7], the larger Y_p of Cr1 is mainly induced by the thicker passive film than Cr0.6. Notably, the decreased Y_p for Cr1.5 should be mainly attributed to the change of the composition rather than the reduced thickness of the passive film. In terms of the resistance R_p, which reflects the corrosion resistance area of the passive film and the electron migration rate at the sample's surface/electrolyte interface, the smaller value of R_p indicates the lower corrosion resistance. Based on this, the corrosion resistance for the four groups of HEAs first decreases and then increases with the increasing concentration of Cr, in line with the results of the polarization tests.

Long-time immersion

Figure 10 shows the surface morphology and average corrosion rate of $Cr_xMnFeCoNi$ HEAs after immersion in a 0.5 M H_2SO_4 solution for 15 days at room temperature. The distribution of the micropores on the surface has no difference from that after polarization tests, but the micropores are much larger and the surfaces become looser. The formation of a more honeycomb-like corrosion surface, especially for Cr1.5, suggests that the HEAs suffered from more severe corrosion during the immersion of the 15 days, due to the absence of the long-term stable passive film. Likewise, the average corrosion rate [Figure 10E] increases exponentially with the Cr concentration. The Cr1.5 HEA shows the highest corrosion rate, 6 times higher than that of Cr1, which seems in contradiction with the results of the electrochemical tests. The significant change in the corrosion behavior during the long-time immersion between the four groups of HEAs could be attributed to the transformed corrosion mechanism. The dominant galvanic corrosion behavior has a direct correlation with the Cr concentration, which would be discussed in detail later.

DISCUSSION

Honeycomb-like morphology after polarization tests

Interestingly, all samples show the honeycomb-like morphology after polarization tests, as shown in

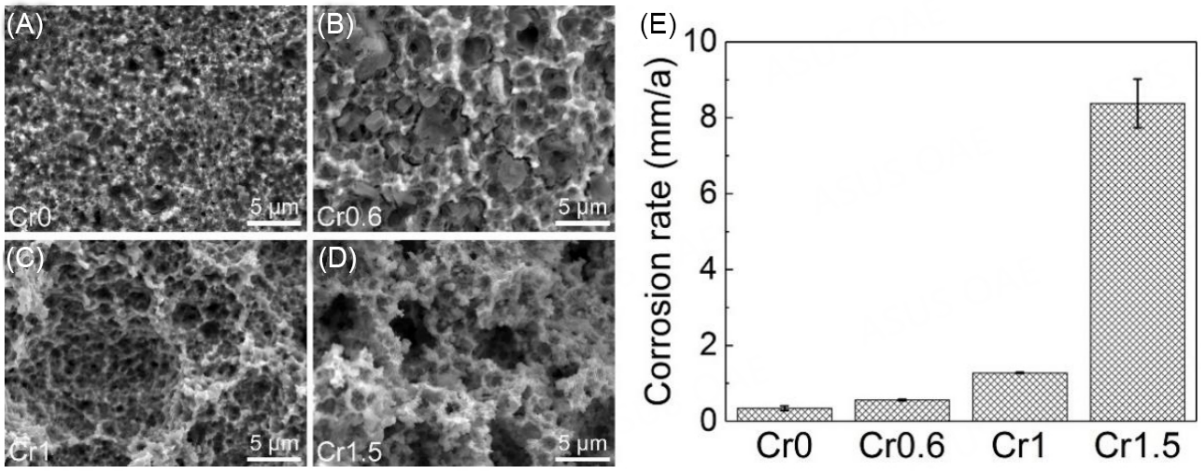

Figure 10. Surface morphology (A-D) and the average corrosion rate (E) by mass loss of the $Cr_xMnFeCoNi$ (x = 0, 0.6, 1, and 1.5) HEAs after immersion in a 0.5 M H_2SO_4 solution for 15 days at room temperature. HEAs: high-entropy alloys.

Figure 6, which means that the corroded micropores were uniformly distributed on the surfaces of $Cr_xMnFeCoNi$ HEAs. A similar phenomenon has also been observed in the Cr1 HEA corroded in H_2SO_4 solution[21,22]. Actually, such corrosion morphology for HEAs can be mainly affected by two factors: (i) the second phase; and (ii) the area of the grain boundaries. Considering that the four groups of HEAs show similar average grain sizes in the range of 312.5-360.6 nm (as shown in Figure 3), the difference in the area of the grain boundaries on the corrosion behavior should be negligible.

With the single fcc phase, the grain boundary has a dominant effect on the corrosion behavior for Cr0, which can act as a defect zone[37,38] and the galvanic corrosion between the grain boundary and the intragranular zone can occur during the corrosion process. Moreover, the grain size of Cr0 is ~ 300 nm, which is close to the diameters of micropores after the polarization tests in Figure 6A. Thus, it is confirmed that the intragranular zone as the anode for Cr0 was preferentially corroded and the grain boundary as the cathode acted as the corrosion barrier at the early stage in H_2SO_4 solution, so that many small micropores were generated on the surface. However, for Cr0.6, Cr1 and Cr1.5, the Cr-rich phase such as $(Cr, Mn)_3O_4$ dissolved out from the matrix, causing a greater impact than the grain boundary on the corrosion behavior. Meanwhile, the corrosion for the Cr-containing HEAs occurred mainly around the $(Cr, Mn)_3O_4$ phase zone and the galvanic corrosion mainly occurred between the second phases and the matrix. With more segregation of the Cr and the increase of the average size of the Cr-rich zone at higher Cr concentration [Figure 1], the galvanic corrosion effect would become stronger as the increasing area ratio of cathode to anode, resulting in the larger and more dispersed micropores in the honey-like morphology [Figure 6]. The depth of the micropores was mainly increased by the galvanic corrosion effect and restrained by the protective effect of the passive film. As more severe galvanic corrosion present in Cr1.5, also indicated by the value of E_{corr}, much deeper micropores were formed on the surface than the other HEAs. The smallest depth of the micropores of Cr1 should be mainly attributed to its dense passive film that has not been damaged by the insufficient galvanic effect at this stage. Moreover, the tiny height fluctuation in or out of the micropores was observed in Figure 6, which may be caused by the galvanic effect between the matrix and the heterogeneous nanoscale particles, such as the (Cr, Mn)-rich phase shown in Figure 4.

Corrosion process during the polarization tests

It is found that when the four groups of HEAs were corroded in the 0.5 M H_2SO_4 solution, the selective dissolution proceeded and the element Co, Ni and Fe were preferentially released from the matrix, which

may be attributed to the dissolution rate difference of the constituent elements in these HEAs in the corrosion environment[7,39]. The hydroxides of Cr, Mn and Fe were deposited on the surface of the HEAs by the hydrolysis reactions at the same time, then some hydroxides formed early in the inner layer may dehydrate to form the oxides[40,41], such as Cr_2O_3. Therefore, the complete passive films were formed. The major chemical reactions present in the above corrosion process are shown as follows:

Anodic reaction: $M \rightarrow M^{n+} + ne^-$ (M: constituent metal element of the HEAs)

Cathodic reaction: $2H^+ + 2e^- \rightarrow H_2$

$O_2 + 2H_2O + 4e^- \rightarrow 4OH^-$

Hydrolysis reaction: $M^{n+} + nH_2O \rightarrow M(OH)_n + nH^+$

Figure 11 shows the schematic diagrams of the corrosion process for these four groups of HEAs during polarization in the 0.5 M H_2SO_4 solution. As discussed above, the intragranular zone near the grain boundary of Cr0 starts to corrode preferentially as the galvanic corrosion effect. With the selective dissolution proceeding, the corroded zone gradually turns into the Mn-rich zone at noble potential, and then the corrosion spreads from the nearest zone to the grain boundary into the grain interior. As the gradually increased area ratio of cathode to anode, the central zone suffers from more severe corrosion than the zone adjacent to grain boundary and the micropores are formed on the surface. Additionally, as described in Figure 11A, more metal ions would be released into the solution than the uncorroded zone by the redox reaction. This would facilitate the hydrolysis reaction to form stable metal hydroxide/oxide, such as Fe and Mn hydroxide/oxide, on the corroded zone, which can retard the corrosion process effectively. Meanwhile, when a small amount of Cr was added in Cr0.6, as shown in Figure 11B, the second phase of $(Cr, Mn)_3O_4$ would precipitate from the matrix, and the corrosion process then occurred near the second phase zone. As the grain boundary can be regarded as the corrosion barrier[38], the corrosion process could end up in the grain boundary zone far away. Notably, such a corrosion process may have two routes: one is that the corrosion propagates along one direction, as the passive film in other directions is more compact; the other one is that the corrosion propagates around the second phase so that the second phase particles would locate in the micropores and peel off from the surface finally. Moreover, the passive film is not only formed in the corroded zone inside the micropores, but also out of the micropores as the slight corrosion by the effect of the nanoscale heterogeneous composition. In terms of Cr1 in Figure 11C, the alloy has the same corrosion mechanism as Cr0.6 except for the microstructure of the passive film. That is, Cr1 has a more compact and thicker passive film than Cr0.6 to provide effective protection to the matrix. However, the micropores for Cr1.5 are much larger and deeper than Cr1 and a few hydroxides/oxides are deposited in the micropores, as shown in Figure 11D. The larger micropores should be due to the larger second phase in the matrix, which would accelerate the corrosion in the local regions without enough protection from the passive film. It can be explained as follows: the dissolution rate of the anode in the micropores is so fast due to the strong galvanic effect that the concentrations of the metal ions are very high; when the diffusion rate of metal cations out of the micropore is much lower than the anodic dissolution rate in the activated region, the concentrations of the metal ions in the micropores could be maintained above a critical value, then the pH value decreases in the local regions by the excessive hydrolysis reactions, and thus causing a more aggressive environment[42,43], which not only restrains the formation of the stable passive film in the micropores, but also induces the formation of the additional (Mn, Cr)-rich layer on the inner surface. In contrast, compared with Cr1, in the larger region outside the micropores of Cr1.5, the more compact and flat passive film following the same passivation mechanism without dissolution process is generated based

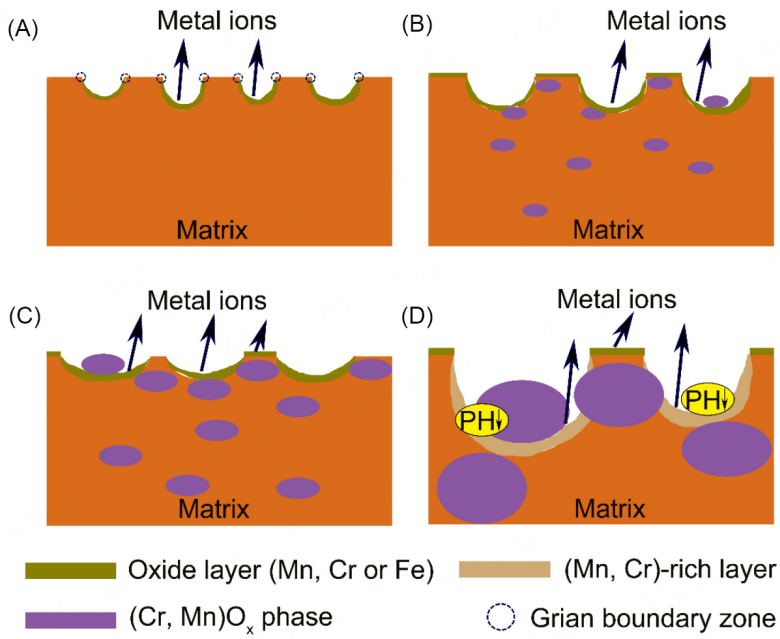

Figure 11. The schematic diagrams of the corrosion process during the polarization tests in 0.5 M H_2SO_4 for Cr0 (A), Cr0.6 (B), Cr1 (C) and Cr1.5 (D).

on the results shown in Figures 6 and 7, which has more effective protection against the matrix, resulting in the lower corrosion rate for Cr1.5 during the polarization tests.

Corrosion process during the long-time immersion tests

It is interesting to find that when the HEAs were immersed in the 0.5 M H_2SO_4 solution at room temperature for 15 days, the corrosion rates increased quickly with the Cr concentration, which seems in contradiction with the results of the polarization tests. This contradiction can mainly be attributed to the competition mechanism between the passivation effect and the galvanic corrosion effect on the honeycomb-like surface. At the early period of the immersion tests, the corrosion behavior can be regarded as the same with the polarization tests[44] and the EIS measurement after 2 h of immersion, as the EIS measurement is at a quasi-stable state and does not change the condition of the corroded surface, when the passivation effect plays an important role in the corrosion process for the samples. Therefore, with the addition of Cr, the stable Cr hydroxide/oxide would be deposited more on the surface, so that the passive film is more compact and thicker. As a result, Cr1.5 has the best corrosion resistance. With the extending time for Cr0, Cr0.6 and Cr1, the etching solution would gradually permeate the passive films in the micropores as the passive films are not very compact and stable. Meanwhile, the composition of the corroded area would convert to the Mn-rich or the (Cr, Mn)-rich region, which increases the area of the cathode. In the end, the enhanced galvanic corrosion effect is strong enough as that of Cr1.5 to increase the depth of micropores so that the passive films in the inner surfaces of the micropores would be dissolved. At this stage, the galvanic corrosion effect for all samples gradually accumulates and starts to transcend the impact of the passivation effect. Subsequently, the micropores continue to grow and the samples are corroded more severely. During this period, pitting-like corrosion is considered to proceed on the honeycomb-like surface, which is also promoted by the loose surface film. Therefore, the galvanic corrosion effect would play a dominant role during the following immersion. As mentioned, the galvanic corrosion would get more severe with the increase of the Cr concentration; hence, Cr1.5 gradually has the highest corrosion rate during the long-time immersion tests. Moreover, the porous structure is also found inside or outside of the micropores of the

samples in Figure 10, which evolved from the tiny height fluctuation during the initial period of the immersion, due to the intrinsic heterogeneous nanoscale particles.

In summary, the addition of Cr in $Cr_xMnFeCoNi$ HEAs is indeed liable to form the Cr oxide in the passive film, which has good stability in the solution and improves the corrosion resistance of the HEAs[17,45]. On the other hand, the Cr can also precipitate from the matrix, which could accelerate corrosion by enhancing the galvanic corrosion effect. In addition, the formed honeycomb-like corroded surfaces on the HEAs would further deteriorate the corrosion resistance. Therefore, it is vital to optimize the matrix structure of the Cr-containing HEAs by changing the constituent elements as well as the processing methods to improve the corrosion resistance in future work. Generally, there are two methods to improve the corrosion resistance of the Cr-containing HEAs. One is to decrease or even eliminate the segregation of the Cr and homogenize the composition and the other is to optimize the structure and the composition of the passive film for high Cr-containing HEAs[46] and eliminate the nanocrystalline-amorphous phase boundaries.

CONCLUSION

The corrosion behavior of ultrafine-grained $Cr_xMnFeCoNi$ HEAs with varying Cr contents in sulfuric acid solution (0.5 M H_2SO_4) was investigated. The Cr-containing HEAs consisted of an fcc matrix and a small amount of $(Cr, Mn)_3O_4$ at the grain boundaries and the (Cr, Mn)-rich phase due to the compositional segregation. During the polarization tests, the corrosion rate first increased and then decreased with the addition of Cr. The Cr1.5 HEA showed the lowest corrosion rate due to the effective passivation. The honeycomb-like surface was formed after electrochemical polarization tests. The passive film was mainly composed of (Mn, Fe) hydroxide/oxide for Cr0 and (Cr, Mn and Fe) hydroxide/oxide for the Cr-containing HEAs. The passive film was more compact and thicker with the increasing Cr concentration. However, the existence of the nanocrystalline-amorphous phase boundaries in the passive film could reduce its stability by providing the diffusion channel of the species. During the static long-time immersion tests, the HEAs showed distinct corrosion behavior from that of the polarization tests, where the corrosion rate increased exponentially from Cr0 to Cr1.5. This unexpected phenomenon should be due to the accumulation of the galvanic corrosion effect induced by the pitting-like corrosion accompanied by the failure of the passivation effect.

DECLARATIONS

Authors' contributions

Conceptualization, methodology, validation, formal analysis, investigation, data curation, visualization, writing - original draft: Wan T
Methodology, investigation: Huang Z
Investigation: Cheng Z, Zhu M, Li Z, Fu D
Methodology, investigation: Zhu W
Conceptualization, methodology, formal analysis, resources, data curation, visualization, writing - review & editing, supervision, project administration, funding acquisition: Ren F

Availability of data and materials

The raw/processed data required to reproduce these findings are available upon request to the corresponding author.

Financial support and sponsorship

This work was financially supported by the National Natural Science Foundation of China (No. 52122102), the Shenzhen Peacock Team Program (No. KQTD2016053019134356) and the Guangdong Innovative &

Entrepreneurial Research Team Program (No. 2016ZT06C279).

Conflicts of interest
All authors declared that there are no conflicts of interest.

Ethical approval and consent to participate
Not applicable.

Consent for publication
Not applicable.

Copyright
© The Author(s) 2023.

REFERENCES

1. George E, Curtin W, Tasan C. High entropy alloys: a focused review of mechanical properties and deformation mechanisms. *Acta Mater* 2020;188:435-74. DOI
2. Otto F, Dlouhý A, Somsen C, Bei H, Eggeler G, George E. The influences of temperature and microstructure on the tensile properties of a CoCrFeMnNi high-entropy alloy. *Acta Mater* 2013;61:5743-55. DOI
3. Zhang Z, Mao MM, Wang J, et al. Nanoscale origins of the damage tolerance of the high-entropy alloy CrMnFeCoNi. *Nat Commun* 2015;6:10143. DOI PubMed PMC
4. Chuang M, Tsai M, Wang W, Lin S, Yeh J. Microstructure and wear behavior of $Al_xCo_{1.5}CrFeNi_{1.5}Ti_y$ high-entropy alloys. *Acta Mater* 2011;59:6308-17. DOI
5. Granberg F, Nordlund K, Ullah MW, et al. Mechanism of radiation damage reduction in equiatomic multicomponent single phase alloys. *Phys Rev Lett* 2016;116:135504. DOI PubMed
6. Shi Y, Collins L, Feng R, et al. Homogenization of Al CoCrFeNi high-entropy alloys with improved corrosion resistance. *Corros Sci* 2018;133:120-31. DOI
7. Chen Y, Duval T, Hung U, Yeh J, Shih H. Microstructure and electrochemical properties of high entropy alloys-a comparison with type-304 stainless steel. *Corros Sci* 2005;47:2257-79. DOI
8. Miracle D, Miller J, Senkov O, Woodward C, Uchic M, Tiley J. Exploration and development of high entropy alloys for structural applications. *Entropy* 2014;16:494-525. DOI
9. Cantor B, Chang I, Knight P, Vincent A. Microstructural development in equiatomic multicomponent alloys. *Mater Sci Eng A* 2004;375-377:213-8. DOI
10. Gludovatz B, Hohenwarter A, Catoor D, Chang EH, George EP, Ritchie RO. A fracture-resistant high-entropy alloy for cryogenic applications. *Science* 2014;345:1153-8. DOI PubMed
11. Sun S, Tian Y, Lin H, et al. Temperature dependence of the Hall-Petch relationship in CoCrFeMnNi high-entropy alloy. *J Alloy Compd* 2019;806:992-8. DOI
12. Sieradzki K, Newman RC. A percolation model for passivation in stainless steels. *J Electrochem Soc* 1986;133:1979-80. DOI
13. Yuan S, Liang B, Zhao Y, Pehkonen S. Surface chemistry and corrosion behaviour of 304 stainless steel in simulated seawater containing inorganic sulphide and sulphate-reducing bacteria. *Corros Sci* 2013;74:353-66. DOI
14. Tan L, Ren X, Sridharan K, Allen T. Corrosion behavior of Ni-base alloys for advanced high temperature water-cooled nuclear plants. *Corros Sci* 2008;50:3056-62. DOI
15. Thomas S, Birbilis N, Venkatraman M, Cole I. Self-repairing oxides to protect zinc: review, discussion and prospects. *Corros Sci* 2013;69:11-22. DOI
16. Qiu Y, Thomas S, Gibson MA, Fraser HL, Birbilis N. Corrosion of high entropy alloys. *NPJ Mater Degrad* 2017;1:15. DOI
17. Xiao D, Zhou P, Wu W, et al. Microstructure, mechanical and corrosion behaviors of AlCoCuFeNi-(Cr,Ti) high entropy alloys. *Mater Des* 2017;116:438-47. DOI
18. Wang R, Zhang K, Davies C, Wu X. Evolution of microstructure, mechanical and corrosion properties of AlCoCrFeNi high-entropy alloy prepared by direct laser fabrication. *J Alloy Compd* 2017;694:971-81. DOI
19. Li QH, Yue TM, Guo ZN, Lin X. Microstructure and corrosion properties of AlCoCrFeNi high entropy alloy coatings deposited on AISI 1045 steel by the electrospark process. *Metall Mater Trans A* 2013;44:1767-78. DOI
20. Hsu Y, Chiang W, Wu J. Corrosion behavior of FeCoNiCrCux high-entropy alloys in 3.5% sodium chloride solution. *Mater Chem Phys* 2005;92:112-7. DOI
21. Ye Q, Feng K, Li Z, et al. Microstructure and corrosion properties of CrMnFeCoNi high entropy alloy coating. *Appl Surf Sci* 2017;396:1420-6. DOI
22. Luo H, Li Z, Mingers AM, Raabe D. Corrosion behavior of an equiatomic CoCrFeMnNi high-entropy alloy compared with 304

stainless steel in sulfuric acid solution. *Corros Sci* 2018;134:131-9. DOI

23. Wang C, Yu J, Yu Y, Zhao Y, Zhang Y, Han X. Comparison of the corrosion and passivity behavior between CrMnFeCoNi and CrFeCoNi coatings prepared by argon arc cladding. *J Mater Res Technol* 2020;9:8482-96. DOI
24. Wang C, Yu Y, Yu J, Zhang Y, Wang F, Li H. Effect of the macro-segregation on corrosion behavior of CrMnFeCoNi coating prepared by arc cladding. *J Alloy Compd* 2020;846:156263. DOI
25. Wang L, Mercier D, Zanna S, et al. Study of the surface oxides and corrosion behaviour of an equiatomic CoCrFeMnNi high entropy alloy by XPS and ToF-SIMS. *Corros Sci* 2020;167:108507. DOI
26. Pang J, Xiong T, Wei X, et al. Oxide $MnCr_2O_4$ induced pitting corrosion in high entropy alloy CrMnFeCoNi. *Materialia* 2019;6:100275. DOI
27. Li S, Dong H, Shi L, Li P, Ye F. Corrosion behavior and mechanical properties of Al-Zn-Mg aluminum alloy weld. *Corros Sci* 2017;123:243-55. DOI
28. Zhang X. Corrosion behavior of Al-3.0 wt.%Mg alloy by cold-drawing process. *Int J Electrochem Sci* 2020:1727-41. DOI
29. Soltis J. Passivity breakdown, pit initiation and propagation of pits in metallic materials - review. *Corros Sci* 2015;90:5-22. DOI
30. Yan Y, Cao H, Kang Y, et al. Effects of Zn concentration and heat treatment on the microstructure, mechanical properties and corrosion behavior of as-extruded Mg-Zn alloys produced by powder metallurgy. *J Alloy Compd* 2017;693:1277-89. DOI
31. Park K, Kwon H. Effects of Mn on the localized corrosion behavior of Fe-18Cr alloys. *Electrochim Acta* 2010;55:3421-7. DOI
32. Zhang B, Wang J, Wu B, et al. Unmasking chloride attack on the passive film of metals. *Nat Commun* 2018;9:2559. DOI PubMed PMC
33. Sun J, Zhang G, Liu W, Lu M. The formation mechanism of corrosion scale and electrochemical characteristic of low alloy steel in carbon dioxide-saturated solution. *Corros Sci* 2012;57:131-8. DOI
34. Rovere C, Alano J, Silva R, Nascente P, Otubo J, Kuri S. Characterization of passive films on shape memory stainless steels. *Corros Sci* 2012;57:154-61. DOI
35. Barsoukov E, Macdonald JR. Impedance spectroscopy: theory, experiment, and applications second edition. Evgenij Barsoukov and J. Ross Macdonald (eds). John Wiley & Sons, Inc., Hoboken, New Jersey, 2005. *J Raman Spectrosc* 2007;38:122. DOI
36. Kissi M, Bouklah M, Hammouti B, Benkaddour M. Establishment of equivalent circuits from electrochemical impedance spectroscopy study of corrosion inhibition of steel by pyrazine in sulphuric acidic solution. *Appl Surf Sci* 2006;252:4190-7. DOI
37. Tachibana S, Kuronuma Y, Yokota T, Yamada K, Moriya Y, Kami C. Effect of hot rolling and cooling conditions on intergranular corrosion behavior in Alloy625 clad steel. *Corros Sci* 2015;99:125-33. DOI
38. Aung NN, Zhou W. Effect of grain size and twins on corrosion behaviour of AZ31B magnesium alloy. *Corros Sci* 2010;52:589-94. DOI
39. Kao Y, Lee T, Chen S, Chang Y. Electrochemical passive properties of AlxCoCrFeNi (x = 0, 0.25, 0.50, 1.00) alloys in sulfuric acids. *Corros Sci* 2010;52:1026-34. DOI
40. Boudin S, Vignes J, Lorang G, et al. Analytical and electrochemical study of passive films formed on nickel-chromium alloys: influence of the chromium bulk concentration. *Surf Interface Anal* 1994;22:462-6. DOI
41. Huang J, Wu X, Han E. Electrochemical properties and growth mechanism of passive films on Alloy 690 in high-temperature alkaline environments. *Corros Sci* 2010;52:3444-52. DOI
42. Li T, Scully JR, Frankel GS. Localized corrosion: passive film breakdown vs. pit growth stability: part iii. a unifying set of principal parameters and criteria for pit stabilization and salt film formation. *J Electrochem Soc* 2018;165:C762-70. DOI
43. Li T, Swanson OJ, Frankel G, et al. Localized corrosion behavior of a single-phase non-equimolar high entropy alloy. *Electrochim Acta* 2019;306:71-84. DOI
44. Shi Z, Liu M, Atrens A. Measurement of the corrosion rate of magnesium alloys using Tafel extrapolation. *Corros Sci* 2010;52:579-88. DOI
45. Asami K, Hashimoto K, Shimodaira S. An XPS study of the passivity of a series of iron-chromium alloys in sulphuric acid. *Corros Sci* 1978;18:151-60. DOI
46. Quiambao KF, Mcdonnell SJ, Schreiber DK, et al. Passivation of a corrosion resistant high entropy alloy in non-oxidizing sulfate solutions. *Acta Mater* 2019;164:362-76. DOI